Excited State Observation of Active K-Ras Reveals Differential Structural Dynamics of Wild-type versus Oncogenic G12D and G12C Mutants

Alexandar L. Hansen,^{1#} Xinyao Xiang,^{2#} Chunhua Yuan¹, Lei Bruschweiler-Li^{1*} and Rafael Brüschweiler^{1,2,3*}

¹Campus Chemical Instrument Center, The Ohio State University, Columbus, Ohio 43210, USA

²Department of Chemistry and Biochemistry, The Ohio State University, Columbus, Ohio 43210, USA

³Department of Biological Chemistry and Pharmacology, The Ohio State University, Columbus, Ohio 43210, USA

The authors contributed equally to this work.

*To whom correspondence should be addressed:

Lei Bruschweiler-Li, Ph.D., E-mail: bruschweiler-li.1@osu.edu

Rafael Brüschweiler, Ph.D., E-mail: bruschweiler.1@osu.edu

Abstract

Despite the prominent role of the K-Ras protein in many different types of human cancer, major gaps in atomic-level information severely limit our understanding of K-Ras function in health and disease. Here, we report the quantitative backbone structural dynamics of K-Ras by solution NMR spectroscopy of the active state of wild-type K-Ras·GTP and two of its oncogenic P-loop mutants, G12D and G12C, using a novel nanoparticle-assisted spin relaxation method, relaxation dispersion and chemical exchange saturation transfer experiments covering the entire range of timescales from picosecond to milliseconds. Our combined experiments allow the detection and analysis of the functionally critical Switch I and Switch II regions that have previously remained largely unobservable by X-ray crystallography and NMR spectroscopy. Our data reveal cooperative transitions of K-Ras·GTP to a highly dynamic excited state that closely resembles the partially disordered K-Ras·GDP state. These results advance our understanding of differential GTPase activities and signaling properties of the WT versus mutants and may thus guide new strategies for the development of therapeutics.

Introduction

Ras proteins belong to a class of GTPase enzymes that play a central role in the early stages of protein signal transduction regulating cell growth, division, and differentiation¹. In its active form, Ras is bound to nucleotide guanosine triphosphate (GTP) and in its inactive state to nucleotide guanosine diphosphate (GDP). Ras enzymatically converts GTP to GDP, a process that is accelerated in the presence of GTPase activating proteins (GAP). Ras genes have been identified as the most frequently mutated oncogenes in human cancer with 19% of all cancers diagnosed in the US associated with Ras mutations and found in 3.4 million cases globally. Furthermore, since 75% of all Ras-associated cancer mutations occur in K-Ras, K-Ras has become the primary focus of Ras cancer research².

Over recent years, X-ray crystallography has provided important information about the 3D structure of K-Ras and its interactions with GDP, GTP and GTP-analogs, and a number of proteins, such as the guanine nucleotide exchange factor (GEF), GAP, and RAF³. The crystal structures also revealed the critical role played by the Switch I (residues 30 - 38) and Switch II (residues 60 - 76) regions in protein-nucleotide interactions. However, while there is a single structure available of the wild-type (WT) K-Ras in an active GTP-bound conformation, most of the Switch regions are missing (Figure 1A)⁴. Nuclear magnetic resonance (NMR) spectroscopy suggests that the homolog H-Ras bound to the non-hydrolyzable GTP-analogue GppNHp is dynamically populating multiple protein substates. Early studies using ³¹P NMR of the nucleotide revealed two states, termed states 1 and 2, slowly exchanging on the NMR chemical shift timescale⁵. State 2 is considered to be competent for downstream binding to effector proteins and the equilibrium between the two states is shifted in favor of state 2 when K-Ras is bound to GTP or GTP γ S^{6,7}. Ras has also been studied via direct observation of some of its backbone NMR resonances. In another study of H-Ras bound to different GTP analogs, extreme NMR line-broadening in the switch regions suggested the presence of conformational dynamics8. A subsequent 15N NMR Carr-Purcell-Meiboom-Gill (CPMG) relaxation dispersion analysis of H-Ras·GppNHp showed that the dynamics is distributed over different protein regions although the properties of the switch regions could not be studied due to broadening of their resonances beyond detection⁹. Despite the missing switch regions, a ¹⁵N conformational exchange saturation transfer (CEST) analysis of H-Ras provided the two substate populations and found large differences depending on whether native GTP or GTP-analogs were used¹⁰. For GTP-bound WT K-Ras and the G12C and G12D mutants

around 80% of the backbone resonances could be assigned recently, but the entire Switch II and a substantial number of resonances of Switch I were still missing¹¹. Because multidimensional NMR applications of Ras when bound to native GTP are impeded by the real-time hydrolysis of GTP, the addition of GEF was shown to significantly extend the lifetime of H-Ras allowing dynamics measurements of a larger number of residues, including several residues of the switch regions¹². A subsequent combined X-ray crystallography and 1D ¹H solution NMR study of WT K-Ras bound to GppCH₂p found a significantly increased state 1 population compared to H-Ras, whereas the K-Ras G12D mutant favors state 2¹³. Together, these studies demonstrated that K-Ras behaves differently than H-Ras with key properties of members of the Ras family being very sensitive to mutations¹⁰. It is therefore important to characterize the structural properties of K-Ras quantitatively and inclusively in its native GTP-bound context to provide a basis for understanding its enzymatic and signaling properties and the differences among the wild-type form and oncogenic mutants.

We report here backbone assignments along with comprehensive dynamics analysis of GTP- and GDP-bound forms of human WT K-Ras4B (residues 1-169) and its oncogenic mutants G12C and G12D, henceforth referred to as K-Ras, including the previously unobservable Switch I and Switch II residues. Experimental conditions for K-Ras·GTP were optimized to make it sufficiently stable over the time course of multidimensional NMR experiments for assignment and dynamics studies. This permitted essentially complete resonance backbone assignments of WT K-Ras·GTP and its G12C and G12D mutants, including the previously elusive yet functionally critical Switch I and II regions. Based on these assignments, the structural dynamics of K-Ras·GTP from picoseconds to milliseconds could be studied at a previously unobtained level of detail using advanced NMR methods that provide unique insights into the function and the free energy landscape of this system. The study reveals highly distinctive dynamic signatures for K-Ras·GTP and K-Ras·GDP in the wild-type and the mutants.

Results

Sample preparation and resonance assignments

Despite years of NMR-based K-Ras research, many residues, including ones in the key Switch I and II regions, could not be detected, and hence not assigned, thereby seriously impeding the structural and dynamic characterization of this protein at atomic detail in solution. By improving the sample preparation and NMR measurement protocol (see Methods section), we could detect and establish essentially complete (>98%) backbone resonance assignments of GTP-bound WT K-Ras and its G12D and G12C mutants at room temperature (298 K). This is illustrated in the 2D ¹⁵N-¹H HSQC NMR spectrum of **Figure 1B** of WT K-Ras showing previously unobservable resonances in Switch I (red) and Switch II (blue). Although some of these peaks are significantly weaker than others or affected by peak overlap, such as D30, Y32, I36, E37 (Switch I) and Q61, E62, E63, Y71, Q79, and Y71 (Switch II), they were amenable to quantitative dynamics analysis. These advances were made possible by the optimized sample preparation protocol, shortened NMR time using non-uniform sampling (NUS) and high sensitivity afforded by measurements at 850 MHz with a TCI cryoprobe. Notably, these results were obtained for intact K-Ras enzyme in the presence of its native GTP substrate with slow hydrolysis of GTP to GDP taking place during the course of the NMR experiment. To prevent t_1 -noise spectral artifacts due to enzymatic turnover changing the sample, the order of the acquisition of increments along the indirect t_1 dimension was randomized and interleaved with the number of scans while making use of minimal phase cycles. The backbone resonance assignments are complete to >98% (the few unassigned residues are listed in **Table S2**). The availability of complete sets of resonances with high spectral quality allowed us to gain previously inaccessible, quantitative insights into the structural dynamics properties of K-Ras and its mutants.

NMR spin relaxation

Backbone ¹⁵N NMR spin relaxation experiments report on conformational dynamics of proteins over a large range of motional timescales. Here, we examined dynamics on the (i) μs – ms processes that are probed by CPMG and CEST experiments^{14,15} and (ii) ps - μs dynamics made accessible by nanoparticles-assisted spin relaxation (NASR)¹⁶ and traditional model-free analysis.¹⁷ **Figure 2** shows representative ¹⁵N CPMG relaxation dispersion and CEST saturation

profiles of residues T35, I36 (Switch I) and E62, Y71 (Switch II). Although these previously unobservable residues give rise to some of the weakest 15 N- 1 H HSQC cross-peaks (**Figure 1B**), they could be unambiguously assigned and fully quantitatively analyzed in both CPMG and CEST experiments as can be seen from the small error bars obtained from repeat experiments. The WT, G12C, and G12D display different amounts of relaxation dispersion, as is visible in **Figure 2A**, reflecting differences in the substate populations, differences in chemical shift changes between ground state and excited state, and the interconversion rate constants $k_{\rm ex}$. High quality 15 N and 1 H CPMG relaxation dispersion data and 15 N-CEST profiles could be measured for all 3 K-Ras variants with 22 to 50 (non-proline) residues showing significant 15 N exchange effects ($R_{\rm ex} > 5$ s⁻¹, **Table 1**). The data were subsequently fit to numerical expressions of conformational exchange using ChemEx¹⁸ software. Quantitative interpretation of the raw data was obtained with a global 2-state exchange process parametrized by an exchange rate constant $k_{\rm ex} = k_{21} + k_{12}$ between the two dynamically interconverting substates 2 and 1 with populations p_2 , $p_1 = 1 - p_2$, and residue-specific chemical exchange differences $\Delta \omega$ (**Table 1**).

At 298 K conformational exchange of K-Ras·GTP follows in excellent approximation a two-site exchange process for all three variants with the global kinetic and thermodynamic parameters depending sensitively on the residue type in position 12 (**Table 1**). On average, exchange proceeds at a moderately slow rate with a relatively large population of the excited state 1, which for WT are $k_{\rm ex} = 400 \, {\rm s}^{-1}$ and $p_1 = 10\%$. Interestingly, both G12D and G12C mutants have lower values in both parameters whereby the G12D mutant has the slowest exchange rate of 301 ${\rm s}^{-1}$ and G12C has the lowest excited state population p_1 of 7%.

Chemical shifts of excited state

The exchange rates $k_{\rm ex}$ fall in a regime on the NMR timescale that allows the quantitative extraction of site-specific ¹⁵N chemical shift changes $\Delta \varpi$ between the ground state 2 and excited state 1 depicted in **Figure 3A,B**. The largest chemical shift changes are observed for residues 29 – 38 (V29, D30, E31, D33, T35, I36, E37, T38) directly preceding or residing in Switch I and residues 54 – 72 (D54, L56, D57, T58, A59, G60, E62, Y64, A66, M67, R68, D69, Q70, Y71, M72) and L79 immediately preceding or residing in Switch II supporting the long-held notion that both Switches play a key role for functionally important conformational dynamics processes of K-Ras. In addition, significant chemical shift changes are observed for the V8, V9, A11, G12X, G13,

and S17 that are either part of or immediately preceding the P-loop. The vast majority of changes occur in the N-terminal effector lobe (residues 1 - 86), whereas in the C-terminal half of K-Ras (residues 87 - 170) changes also occur but are overall much smaller and more scattered across the primary sequence (**Figure S1**).

Determination of the conformation or conformational ensemble of the excited state is difficult based on backbone 15N, 1HN chemical shift information alone. However, it is possible to compare the chemical shifts of the excited state with those of alternative, experimentally established states or with predicted chemical shifts to draw conclusions about their structural similarity with the excited state (Figure 3C-G). Such a comparison is depicted in Figure 3G between the 15N chemical shifts of the excited state of all residues of K-Ras·GTP and the equilibrium chemical shifts of K-Ras·GDP yielding close agreement with a high Pearson R^2 correlation of 0.88. When limiting this comparison only to signed $\Delta \varpi$ values observed for residues that belong either to Switch I (**Panel 3C**) or Switch II (**Panel 3D**), the R² values are 0.95 and 0.69, respectively (Table 2). An alternative model is a random coil model for Switch I and II (Panels 3E,F), with random coil chemical shifts predicted based on the amino-acid sequence using the POTENCI¹⁹ software resulting in reduced R^2 correlations of 0.88 and 0.47. This analysis shows that the excited state of K-Ras·GTP adopts a state that resembles K-Ras·GDP with a degree of flexibility for parts of Switch I and Switch II similar to that of a random coil conformation. Residues that deviate most from the K-Ras·GDP model in Figure 3G are those that are closest to the γ -phosphate of GTP therefore experiencing additional chemical shift changes that are likely caused by the change of chemistry between GTP and GDP rather than structural dynamics (Figure S2).

Nanoparticle-assisted spin relaxation

Relaxation dispersion and CEST data reflect conformational exchange on the millisecond timescale whereas 15 N- R_1 and R_2 relaxation parameters inform about additional dynamic processes of N-H bond vectors occurring on faster timescales. We used the nanoparticle-assisted spin relaxation method (NASR) method, which measures the change of transverse R_2 relaxation in the presence and absence of silica nanoparticles to report directly on ps- μ s motions 16 . The extracted S^2 (NASR) order parameters are shown in **Figure 4A,B** for the three variants of K-Ras·GTP and K-Ras·GDP. For all forms, regular secondary structures are internally rigid as reflected in high

 $S^2(NASR)$ order parameters whereas the N- and C-termini have increased mobility (low $S^2(NASR)$) as is typical for many proteins. Also, loop residues E107 – V109 and S122 – R123, which are located in the C-terminal half of K-Ras, exhibit increased mobility across all forms. For K-Ras·GTP moderately increased mobility is found for Switch II residues with several residues $S^2(NASR) < 0.6$ whereas Switch I residues are motionally restricted with $S^2(NASR) > 0.68$. For K-Ras·GDP, the NASR profiles change significantly showing increased mobility in Switch I, especially for E31, Y32 with $S^2(NASR)$ between 0.50 and 0.61, and even larger amplitude motions for Switch II residues G60 - S65 with $S^2(NASR)$ between 0.21 and 0.37 for WT. The NASR profiles of the mutants closely resemble those of the WT except for G12D, which for residue G60 of K-Ras·GDP is significantly more rigid ($S^2(NASR) = 0.55$) than WT and G12C ($S^2(NASR) = 0.33-0.38$). For A59, G12C is more flexible than WT and G12D ($S^2(NASR) = 0.67$ vs 0.82 and 0.85).

The secondary structure propensities²⁰ (SSP) of all three variants for the GDP- and GTP-bound forms are shown in **Figures 4C,D** with the largest differences between the GDP and GTP-bound forms occurring in Switch I and Switch II. In K-Ras·GDP, Switch I residues P34 and T35 have SSP indices close to zero, which is consistent with a high degree of intrinsic disorder, whereas in K-Ras·GTP the same residues have a value of about 0.32-0.42 indicative of a more structured state. Similarly, Switch II residues E62 – A66 have systematically smaller (absolute) values in K-Ras·GDP than in K-Ras·GTP suggesting that this section of Switch II is overall significantly more disordered in the GDP-bound form. From residue M67 onward, Switch II becomes better structured with the apex of the SSP index approaching 1 around residue 70 for both nucleotide ligands. This interpretation is consistent with the NASR dynamics results and closely mirrors results obtained by TALOS-N²¹ software (**Figure S3**).

Discussion

State 2 vs. state 1 of K-Ras

Ever since the discovery by ³¹P NMR⁵ that K-Ras·GTP populates an alternative state 1 distinct from its major state 2, the biological roles and structural properties of the two states have been of intense interest. Variations of the equilibrium constant between the two interconverting states for different small GTPases and their interactions with effector proteins have been associated

with different biochemical properties^{22–25}. In particular, it is known that state 1 promotes nucleotide exchange while inhibiting interactions with downstream effector proteins, whereas state 2 allows effector binding and GTP hydrolysis. States 1 and 2 were subsequently structurally characterized by X-ray crystallography of selected K-Ras mutants bound to GDP or GTP analogs^{26,27}, but detailed structural dynamic information of K-Ras bound to the native GTP ligand in solution remained elusive. Such information is critical since the crystal structures do not necessarily reflect the substates present in solution. Based on the equilibrium constants⁶ between state 2 and state 1, we assigned the dominant ground state observed in our CPMG and CEST experiments to state 2 and the excited state to state 1. This is further supported by the structural dynamic characteristics of the ground versus excited state in the context of the known functional properties of states 1 and 2 described below.

Although the Switch I and II regions of K-Ras have been known to make critical contacts to the GTP substrate and are important for GTPase activity, they have remained largely undetectable by X-ray crystallography and solution NMR. By optimizing NMR samples and experimental conditions, we have been able to detect and assign essentially all backbone chemical shifts of both Switch I and II for K-Ras·GTP WT, G12D, and G12C. Specifically, 100% of the non-proline residues could be assigned for G12D and 98% for WT (missing assignments: Y64, S65, M72) and G12C (missing assignments: Q61, Y64, M72) (see **Table S2**). They allowed the quantitative capturing of the dynamics of a large number of previously unobservable residues in Switch I and II.

Global 2-state exchange and free energy diagram of K-Ras·GTP and its mutants

CPMG and CEST data sensitively report on conformational exchange on the biologically significant millisecond timescale allowing screening for one or several transiently populated alternative conformational states that are in dynamic equilibrium with the main state. CEST experiments are complimentary to CPMG as they directly depict both the magnitude and the sign of the chemical shift of the excited state, i.e., whether it is up-field or down-field shifted relative to the ground state. This is important when modeling the structure of the excited state with alternative structural states as discussed below. The CEST data of K-Ras-GTP unambiguously show the existence of a single excited state, which is manifested by the presence of a second dip in the CEST profiles of a sizable number of residues as illustrated in **Figure 2** for T35 in Switch I

and E62 in Switch II. Even for E62, which gives rise to the weakest cross-peak in the entire HSQC spectrum (lower left corner of Figure 1B), the presence of an excited state of this residue is evident for all three K-Ras-GTP variants (Figure 2D). Within the NMR detection limits there is no indication that any residue substantially populates more than one excited state on the µs-ms timescale. The CPMG and CEST data of all three K-Ras·GTP variants could be fit to global 2state exchange processes for WT and both mutants with best fitting model parameters listed in Table 1. K-Ras-GTP undergoes thermally activated, stochastic transitions between a dominant conformational state (ground state) and an alternative conformational state (excited state) cooperatively involving Switch I, Switch II, the P-loop and few other regions discussed further below. WT-K-Ras behaves distinctly with both $k_{21} = 40.6$ s⁻¹ and $p_1 = 10.1\%$ being elevated compared to its oncogenic mutants G12D ($k_{21} = 27.1 \text{ s}^{-1}$ and $p_1 = 9.0\%$) and G12C ($k_{21} = 22.7 \text{ s}^{-1}$ and $p_1 = 7.0\%$). Hence, WT K-Ras has an excited state that is more accessible both thermodynamically (larger p_1) and kinetically (larger k_{21}) than the oncogenic mutants which may be instrumental for the reduced GTPase activity of mutant K-Ras (vide infra). The corresponding free energy diagram of the three K-Ras variants is depicted in Figure 5 highlighting distinct differences in populations and the free energy of the transition state of the WT vs. mutants. In contrast to K-Ras·GTP, we find no experimental evidence that K-Ras·GDP undergoes conformational exchange on the millisecond timescale with a significantly populated excited state (Figure S4).

The residues participating in conformational exchange of K-Ras·GTP are located predominantly in the N-terminal effector lobe (**Figure 3A,B**). These residues are V8, V9, A11, G12X, and G13 in the P-loop, residues N29 – E40, which essentially represent the entire Switch I, residues D54 – M72, constituting a good part of Switch II, and L79 and C80 of the β 4-strand. G12X and G13 display notable differences in $\Delta \omega$ among WT and the mutants, whereas for most other residues WT and the two mutants experience similar $\Delta \omega$. This is not surprising as G12X is the mutation site and, hence, residues in this region experience a different chemical environment that is reflected in the chemical shifts of the ground state, the excited states, and their differences. Residues 92 - 98 belonging to the C-terminal end of the α 3-helix in the C-terminal allosteric lobe (residues 87 – 166) display somewhat more modest exchange-induced chemical shift modulations. Since the P-loop is wedged between residues 92-98 and L79/C80 of β 4-strand on one side and the GTP ligand on the other, the dynamic modulation of the P-loop during exchange requires

adjustments in the local structure and environment of the α 3-helix and β 4-strand residues manifested in the observed chemical shift changes. These latter regions of the α 3-helix and β 4-strand likely represent allosteric sites and it may be possible to modulate K-Ras signaling by targeting them with ligands that stabilize the excited state (state 1) thereby disrupting interactions of K-Ras·GTP with downstream effector proteins.

Intrinsic differences between K-Ras state 2 and state 1 structure and dynamics

Not only do the CPMG and CEST experiments provide global exchange dynamics parameters, but they also return residue-specific chemical shift differences $\Delta \varpi$ between the two states shedding light on the structure of the excited state. A direct way to annotate $\Delta \varpi$ values is by comparing them with chemical shifts that are known or expected for alternative states. The best agreement is found when using the conformational ensemble of K-Ras·GDP as a model for the excited state with Switch I behaving as random coil (**Figure 3**). This is consistent with SSP data that are close to zero for Switch I of K-Ras·GDP²⁸ (indicative of random coil) (**Figure 4D**), whereas for K-Ras·GTP the corresponding SSP values are clearly elevated for residues positioned toward the middle of Switch I (**Figure 4C**). This conclusion is supported by NASR S^2 data of K-Ras·GDP (**Figure 4B**) providing direct evidence that Switch I is substantially more flexible than in K-Ras·GTP. It further corroborates our experimental finding that Switch I of K-Ras·GTP undergoes a major transition between a structured ground state and a floppy excited state that behaves like K-Ras·GDP.

For the initial part of Switch II (residues G60 - S65), the SSPs of K-Ras·GDP are also close to zero before they start to markedly rise from residue A66 onward. The NASR profile (**Figure 4B**) shows strikingly low S^2 (NASR) order parameters for this initial part ranging between 0.21 - 0.39 before they rise to values between 0.66 and 0.90 for the rest of Switch II (residues 66 - 76). By contrast, NASR dynamics of K-Ras·GTP is much more constrained with S^2 values ranging between 0.6 and 0.9 (**Figure 4A**). For both Switch I and Switch II, K-Ras·GDP is a suitable model of the excited state of K-Ras·GTP suggesting a conformational exchange behavior where both switches have limited flexibility in the ground state and significantly more heterogeneous dynamics in the excited state with the N-terminal parts of both Switch I and II being most dynamic. Of relevance, only limited dynamics is observed for the two switch regions by traditional model-free S^2 order parameter analysis (**Figure S5**). It shows the extended range of

dynamics information provided by NASR indicating that the Switch dynamics takes place on the $10 \text{ ns} - 1 \text{ µs timescale}^{16}$.

Minimal X-ray structural ensemble models of K-Ras·GDP

There is no experimental structural ensemble of the dynamics observed in Switch II of K-Ras·GDP in solution. However, many X-ray crystal structures of WT K-Ras·GDP exist with their Switch II structures differing by a variable degree from each other. With these, one can construct ensembles of interconverting crystal structures to interpret the experimental $S^2(NASR)$ profiles. In particular, the different orientations of the Switch II-α2 helix adopted by the two WT structures (PDB entry $40BE^{29}$ and $6MBU^{30}$) can explain the positive S^2 (NASR) gradient observed between residues A66 and E76. Furthermore, the pronounced S²(NASR) minimum in the Switch II loop region requires the presence of the G12D mutant structure 4EPR³¹ in addition to the WT K-Ras · GDP conformations found in crystal structures (Figure S6B). For Switch I, the vast majority of the reported K-Ras·GDP X-ray crystal structures (reviewed, e.g., in Ref. 32) adopt the same conformation except for the D33E (PDB 6ASA) and A59G (PDB 6ASE) mutants, where 6ASA and 6ASE possess nearly identical and more extended Switch I conformations³³. The characteristic $S^2(NASR)$ profile can be accounted for only if one assumes significant populations from at least three conformers, namely WT 6MBU, G12D mutant 4EPR, and A59G mutant 6ASE with populations 47%, 39%, and 14%, respectively (Figure 6). This is the minimal ensemble found to best reproduce the S^2 (NASR) profile, whereas the introduction of the other WT structure 4OBE did not show significant further improvement (Figure S6E). This ensemble closely reflects the S²(NASR) profile for the Switch II region except for G60. For Switch I, the agreement is best for residues D30, E31, D33, and E37 and it somewhat overestimates S2 for residues Y32, D38, and S39. Furthermore, it underestimates S^2 for N26, where the differences between 6MBU and 6ASE at the end of the α 1-helix lead to lowered S^2 values, whereas S^2 (NASR) suggests a more rigid behavior for residues immediately preceding D30. This analysis shows how the diverse set of Xray crystals available for K-Ras-GDP can serve as realistic templates for interconverting conformers in solution on the sub-us time scale. Such structural ensembles can be further refined by molecular dynamics (MD) computer simulations using the experimental $S^2(NASR)$ data as quantitative benchmarks (see below).

WT K-Ras·GTP is more dynamic than G12D and G12C

Our study reveals the structural nature of the two significantly populated and functionally distinct substates 1 and 2 of K-Ras·GTP in solution. Based on its backbone 15 N chemical shifts, the excited state 1 is K-Ras·GDP-like exhibiting high flexibility for specific portions of Switch I and II. This is in contrast to the ordered, structurally much better organized state 2, which in terms of signaling corresponds to the active state of K-Ras as it is binding competent with respect to downstream effector proteins. The NMR results show that WT K-Ras·GTP is dynamically more active compared to the oncogenic mutants G12D and G12C by having the highest population of its excited state 1 together with the highest k_{21} rate constant between the ground state (state 2) to the excited state 1. Together with the P-Loop, Switch I and Switch II undergo the largest structural-dynamic transformations as the protein is shuttling between the two states. The dynamic activities of WT, G12C, and G12D characterized here correlate with their respective GTPase turnover rates 34,35 ranging between 4.03×10^{-5} s⁻¹ (WT) and 1.13×10^{-5} s⁻¹ (G12C).

The excited state of K-Ras·GTP is highly dynamic and K-Ras·GDP-like

The correlations of **Figure 3C,D** and **G** are high, but not perfect. This should not be a surprise since K-Ras·GDP and the K-Ras·GTP excited state 1 differ chemically by the absence or presence of the γ -phosphate group of the nucleotide, which can cause significant chemical shift changes of surrounding residues without necessarily involving structural changes. Indeed, those residues that deviate the most in **Figure 3G** belong in regions with the closest proximity to the γ -phosphate (**Figure S2**). Taken together, our CPMG/CEST results show that the excited state of K-Ras·GTP is K-Ras·GDP-like with Switch I, adopting in good approximation a random coil state. It should be noted that although the excited state of K-Ras·GTP is highly dynamic, the S^2 (NASR) profile shows only slightly reduced S^2 values in Switch I and II compared to the rest of the protein (**Figure 4A**). This is because of the dominance of the ground state of K-Ras·GTP ($p_2 = 90\%$) that is much more ordered in both switch regions.

The results help rationalize why the dominantly populated K-Ras·GTP ground state corresponds to state 2 whereas the excited state is state 1 along with their distinct mechanistic roles. Because of its K-Ras·GDP-like nature, state 1 is capable to mimic the known functional behavior of K-Ras·GDP both in its favorable interactions with GEF for nucleotide exchange and its biological inactivity by preventing interactions with effector proteins. By contrast, state 2 is the

active state of K-Ras·GTP that interacts with effectors enabling downstream signaling. The K-Ras mutants G12C and G12D have a higher population of state 2 vs state 1, which makes them more competent for effector interactions further compounding their diminished GTPase activity. This amplifies the signaling activity of the mutants that is the root cause of their oncogenicity.

The observed excited state dynamics can also help better understand K-Ras from an enzymatic perspective. NMR-based observations of the spontaneous sampling of excited state conformations in enzymes have been identified as critical components for catalysis^{36–39}. For example, for dihydrofolate reductase (DHFR) excited conformers of a series of ground states along the reaction pathway were found to correspond to structures belonging to states that immediately follow in the cycle⁴⁰ or for arginine kinase, the excited state of the Michaelis complex was found to adopt the structure of the transition-state analog of the phosphorylation reaction of the arginine substrate⁴¹. The similarity between the excited state 1 of K-Ras·GTP and the product of the GTPase reaction, K-Ras·GDP, follows the same pattern, with k_{21} (40.6 s⁻¹) significantly faster than k_{cat} , which in the absence of GTPase activating protein (GAP) is less than $4x10^{-5}$ s⁻¹. 34,35,42</sup> This suggests that while it stochastically samples the product-like K-Ras·GDP state, K-Ras·GTP successfully undergoes GTP-hydrolysis only once every 10⁷ transitions. This low enzymatic efficiency, which is a hallmark of K-Ras, is the reason why WT K-Ras requires the help of GAP to accelerate turnover. When interacting with GAP and effector proteins like RAF1, 43 K-Ras-GTP must be in state 2 and not state 1 as binding to GDP-bound like state 1 would also allow binding to K-Ras·GDP thereby abolishing the signaling selectivity of the active state.

Synergies between NMR and MD simulations

Over the years, numerous computational studies have been reported with the goal to elucidate the functional properties of Ras proteins in relationship to experiment.⁴⁴ Early studies focused mostly on H-Ras,^{45–47} but due to its distinct behavior those findings cannot be directly transferred to K-Ras, which was also confirmed by computation.^{47,48} An extensive molecular dynamics (MD) simulation study of WT K-Ras and its G12 mutants in their GDP and GTP-bound forms found substantial amounts of dynamics in the switch regions, with other protein areas sampling distinct substates, but there were no significant changes in dynamics observed between WT and its mutants nor between GTP and GDP-bound states of the same mutant⁴⁹. Hence, past

simulations have been unsuccessful in revealing distinct dynamics differences between the GTPand GDP-bound states reported here.

While MD simulations of K-Ras.GDP can start from well-defined X-ray crystal structures,⁵⁰ K-Ras·GTP represents a major challenge for MD due to the lack of complete experimental structures as starting points. Starting structures for MD have been constructed by simply replacing GDP by GTP in a K-Ras.GDP structure⁴⁹, modeling in missing residues followed by docking simulations of GTP to the structure,⁵¹ or by using X-ray structures of the PDB Q61H mutant bound to a GTP-analog⁵². These procedures clearly introduce an amount of uncertainty in the initial structure with consequential impact on the simulation outcome.

An equally important challenge has been the validation of the ensuing MD trajectories, especially for the functionally vital switch regions that have been unobservable by both NMR and crystallography. The essentially complete, quantitative body of experimental data of the backbone structural dynamics of K-Ras presented here covering both switches provides key benchmarks for molecular modeling, including MD, of K-Ras. It will allow the critical assessment of MD trajectories and other conformational ensembles of K-Ras and its mutants in their GTP and GDP bound states. Although $k_{\rm ex}$ between states 2 and 1 is too slow to be captured by traditional MD simulations, the site-specific CPMG/CEST derived chemical shift information (Figure 3) of the two states will allow critical comparisons between experimental and predicted chemical shifts^{50,53}. Such information should allow the generation of more realistic conformational ensembles of K-Ras-GTP in its ground and excited states thereby deepening our understanding of its diverse functional behavior. These ensembles along with the sample preparation protocol introduced here for detection and assignments of the switch resonances should prove powerful for future investigations, such as ligand screening toward the development of drugs that bind to specific pockets of K-Ras mutants⁵⁴ and for studying at atomic detail the structure and dynamics of the interactions of K-Ras with GEF, GAP, and a myriad of effector proteins.

Acknowledgements

We thank Dr. Dehua Pei for providing the wild-type K-Ras plasmid and Dr. Jiaqi Yuan for assisting in the cloning of the K-Ras mutants (both at the Department of Chemistry and Biochemistry, The Ohio State University). This work was supported by the U.S. National Science

Foundation (MCB-2103637). All NMR experiments were performed at the CCIC NMR facility at The Ohio State University. The funders had no role in study design, data collection and analysis, decision to publish or preparation of the manuscript.

Author contributions

L. B.-L. and R. B. conceived and designed the project. L. B.-L. prepared all K-Ras samples. A. L. H. developed the experimental CPMG and CEST approach and performed their analysis. X. X. performed and analyzed the NASR experiments. C. Y. performed and analyzed all resonance assignment experiments. R. B. wrote the first manuscript draft. All authors contributed to the manuscript writing.

Competing Interests Statement

The authors declare no competing interests.

Tables

Table 1. Summary of NMR-based dynamics results of WT, G12C, and G12D K-Ras bound to GTP at 298 K. Uncertainties in the parameters were determined through bootstrap analysis.

Sample		¹⁵ N CPMG ^a	¹ H ^N CPMG ^a	¹⁵ N CEST ^a	k_{21} (s ⁻¹)	k_{12} (s ⁻¹)	$k_{\rm ex}$ (s ⁻¹) ^b	p ₁ (%) ^c
GTP	WT	29	22	28	40.6 ± 2.2	359 ± 11	400 ± 12	10.15 ± 0.47
	G12C	31	-	31	22.7 ± 0.9	303 ± 10	326 ± 11	6.97 ± 0.17
	G12D	50	22	50	27.1 ± 2.0	274 ± 16	301 ± 17	9.00 ± 0.44

^a Total number of residues with significant conformational exchange contributions that were included in parametrization of 2-site exchange model by global non-linear least squares fitting.

^b Globally fitted exchange rate constant $k_{\text{ex}} = k_{21} + k_{12}$ using a two-state conformational exchange model consisting of a ground state ('state 2') and an excited state ('state 1').

^c Globally fitted population p_1 of the excited state ('state 1') whereby $p_1 = 1 - p_2$.

Table 2. Summary of excited state chemical shift correlations shown in Figure 3.

	Switch	I: 29-37	Switch	Effector lobe: 1-86	
abscissa	$\Omega_{ m RC}$ - $\Omega_{ m GTP,2}$	$\Omega_{ ext{GDP}}$ - $\Omega_{ ext{GTP,2}}$	$\Omega_{ m RC}$ - $\Omega_{ m GTP,2}$	$\Omega_{ ext{GDP}}$ - $\Omega_{ ext{GTP,2}}$	$\Omega_{ ext{GDP}}$
rmsd	2.10 ppm	3.05 ppm	3.39 ppm	1.56 ppm	2.15 ppm
R ²	0.875	0.951	0.473	0.686	0.881

Figure Legends

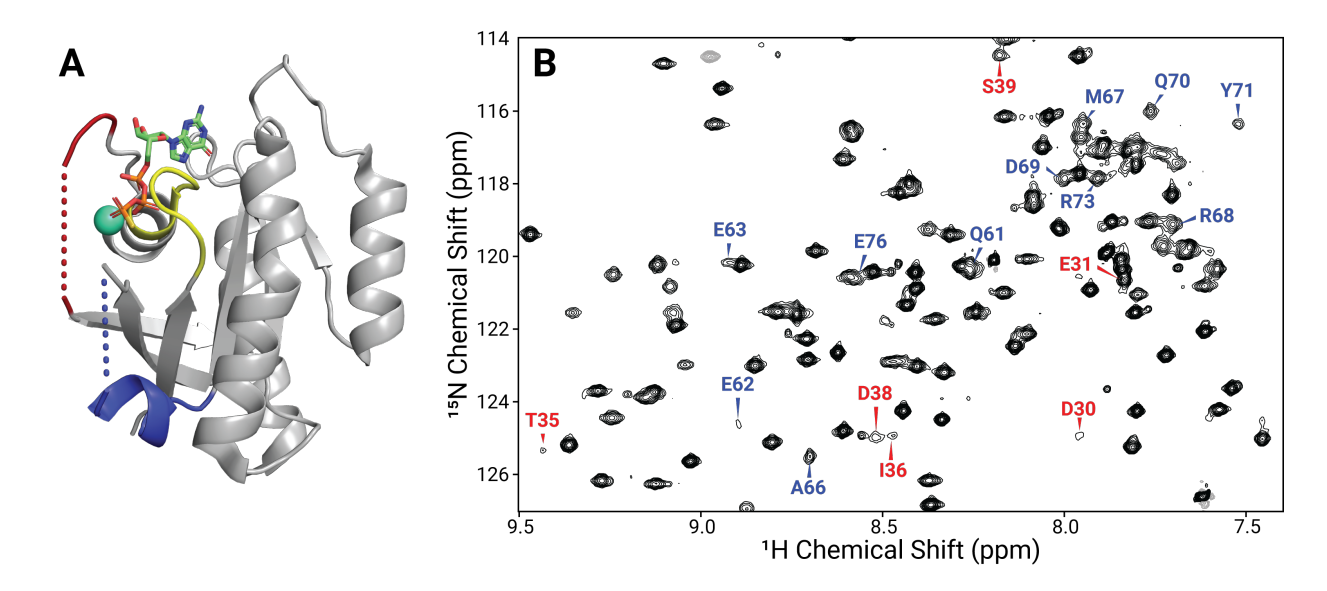


Figure 1. Depiction of the X-ray crystal structure of the GTP-form of wild-type K-Ras and a representative solution NMR amide spectrum. **A)** X-ray crystal structure of WT K-Ras·GTPγS (PDB entry: 5VQ6) where large sections of Switch I (red) and Switch II (blue) are missing. **B)** A section of the reference spectrum from the ¹⁵N CPMG relaxation dispersion data of WT K-Ras·GTP highlighting some of the assignments of residues from Switch I (red) and Switch II (blue), many of which have previously been unobservable.

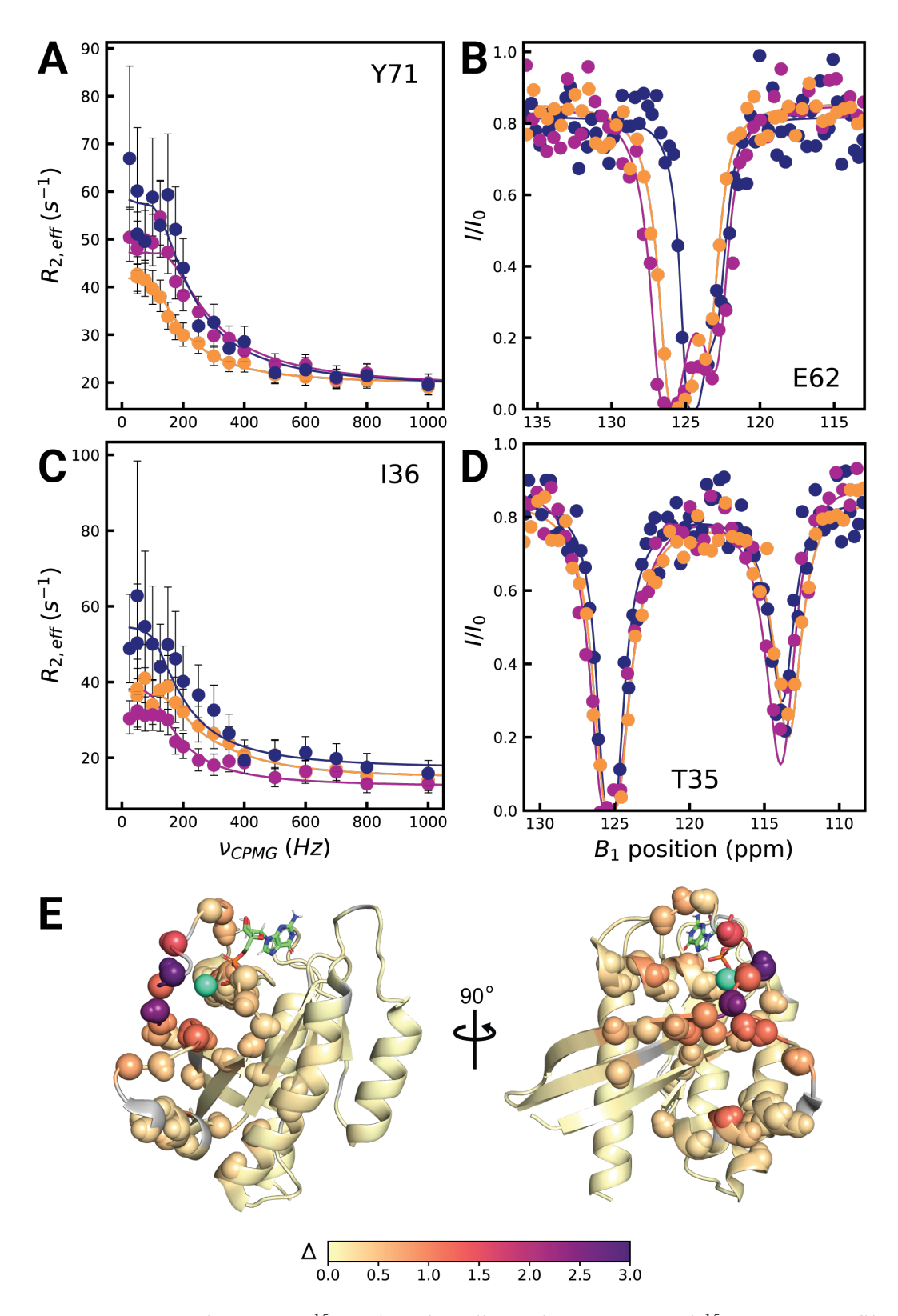


Figure 2. Representative NMR ¹⁵N-relaxation dispersion curves and ¹⁵N CEST profiles for K-Ras·GTP with results color-coded on 3D structure of K-Ras. ¹⁵N-dispersion and CEST profiles are shown for WT (dark blue), G12D (purple) and G12C (orange) K-Ras bound to GTP. **A**)

Representative Switch II ¹⁵N CPMG dispersion. Values of R_{2,eff} were calculated as described in Supporting Information with errors derived from error propagation of the experimental uncertainties in signal amplitudes. Data are presented as the measured value ± one standard deviation. B) Representative Switch II ¹⁵N CEST profiles. C) Representative Switch I ¹⁵N CPMG dispersions and presented as described in A. D) Representative Switch I ¹⁵N CEST profiles. E) The combined excited state chemical shift difference Δ for WT K-Ras·GTP is plotted on the K-(PDB ID: 4OBE) for Ras-GDP structure all residues, where $\Delta =$ $\sqrt{\left(\frac{\Delta\omega_N}{\sigma_N}\right)^2 + \left(\frac{\Delta\omega_{HN}}{\sigma_{HN}}\right)^2}$, and σ_N and σ_{HN} are the standard deviations of amide ¹⁵N and ¹H^N chemical shifts with values 5.218 ppm and 0.634 ppm, respectively. Residues with $\Delta > 0.2$ are shown as spheres while unobserved residues are shown in grey. The teal sphere is the Mg2+ ion observed in the crystal structure.

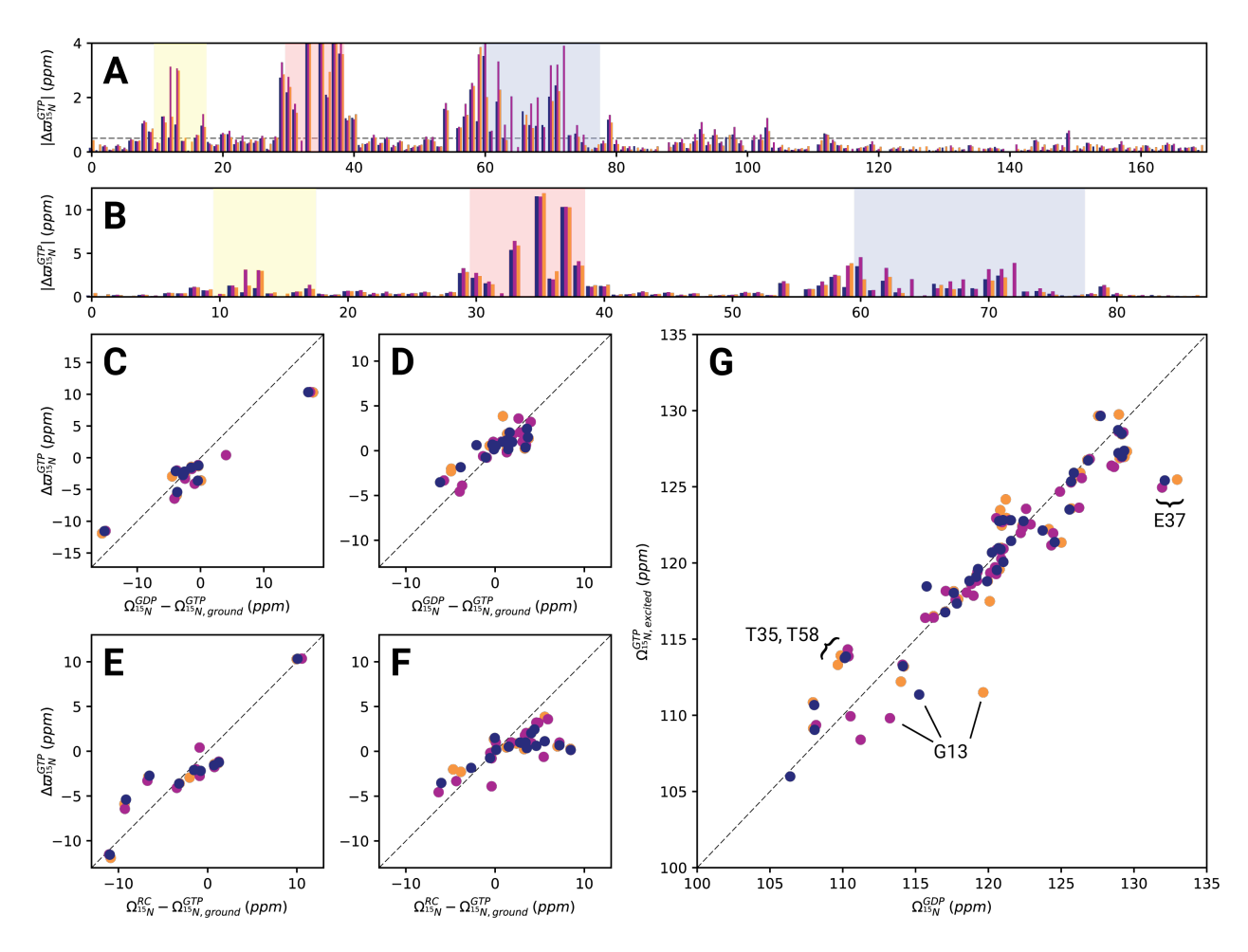


Figure 3. Relating ¹⁵N NMR chemical shifts of excited state of K-Ras·GTP to alternative states of K-Ras. In all panels, data shown for K-Ras·GTP for WT, G12D, and G12C are colored dark blue, purple, and orange, respectively. **A)** Unsigned ¹⁵N dynamic chemical shift differences $|\Delta\varpi|$ between excited and ground states, obtained from CPMG and CEST experiments (see Methods Section), are plotted against the primary sequence. The dashed line in panel A is at 0.5 ppm while the P-loop, Switch I, and Switch II regions are highlighted in yellow, red, and blue, respectively. **B)** Same as in A but highlighting the effector lobe residues. **C)** Signed ¹⁵N $\Delta\varpi$ values of Switch I residues correlated with the equilibrium chemical shift differences observed between the ¹⁵N-¹H HSQC spectra of K-Ras·GDP and K-Ras·GTP. **D)** Same as C but showing Switch II residues. **E)** The corresponding correlations of Switch I ¹⁵N $\Delta\varpi$ values with the differences between chemical shifts predicted for random coil states and those observed for K-Ras·GTP. **F)** Same as E but showing Switch II residues. **G)** Depiction of the correlation between the chemical shifts of the excited state of K-Ras·GTP and K-Ras·GDP for residues 1-86 with ¹⁵N $|\Delta\varpi|$ > 0.5 ppm. The dashed lines in Panels C-G correspond to the diagonal with slope 1. RMSD and Pearson R^2 correlation coefficients are provided in Table 2. Errors in the measurements are smaller than the symbol sizes.

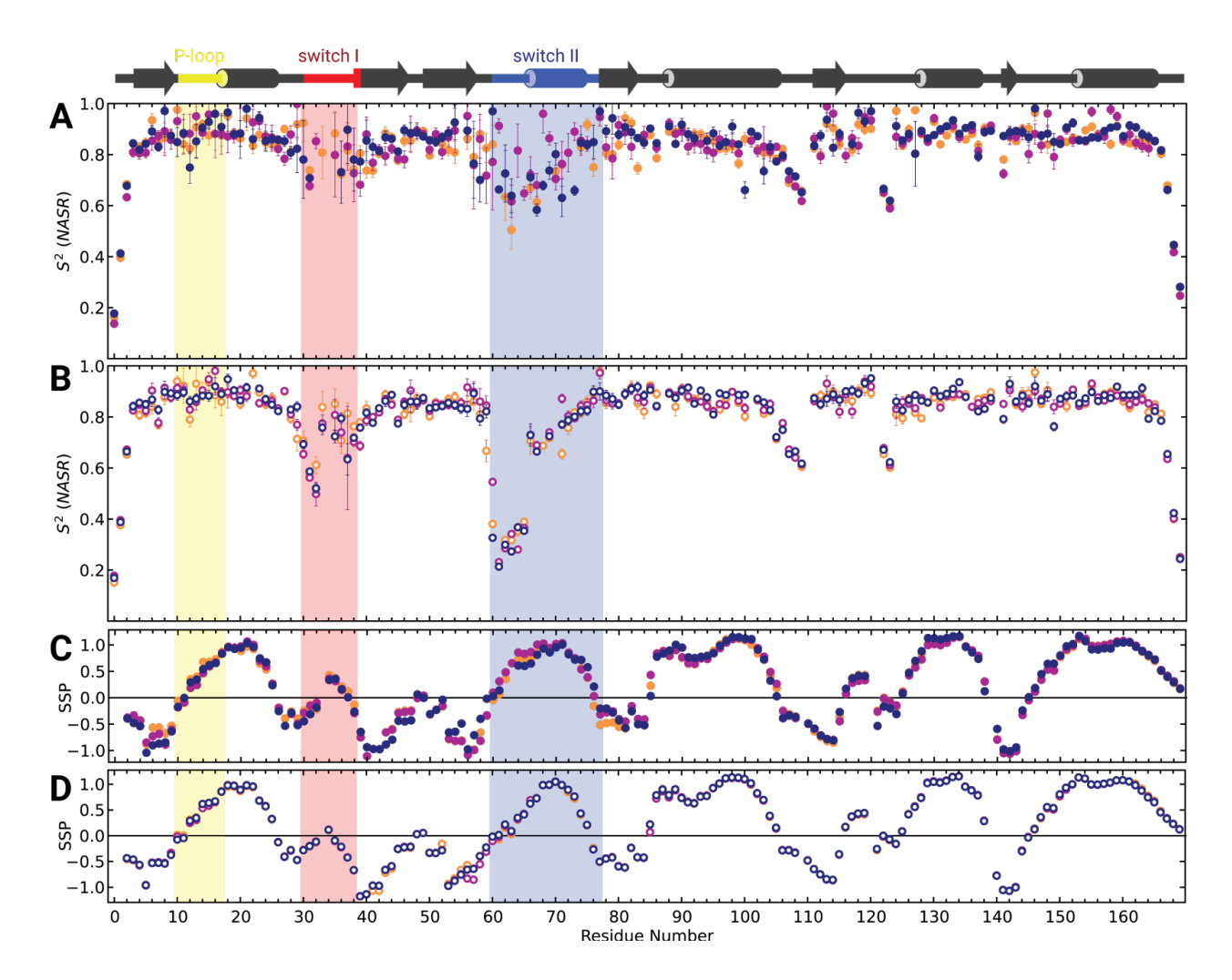
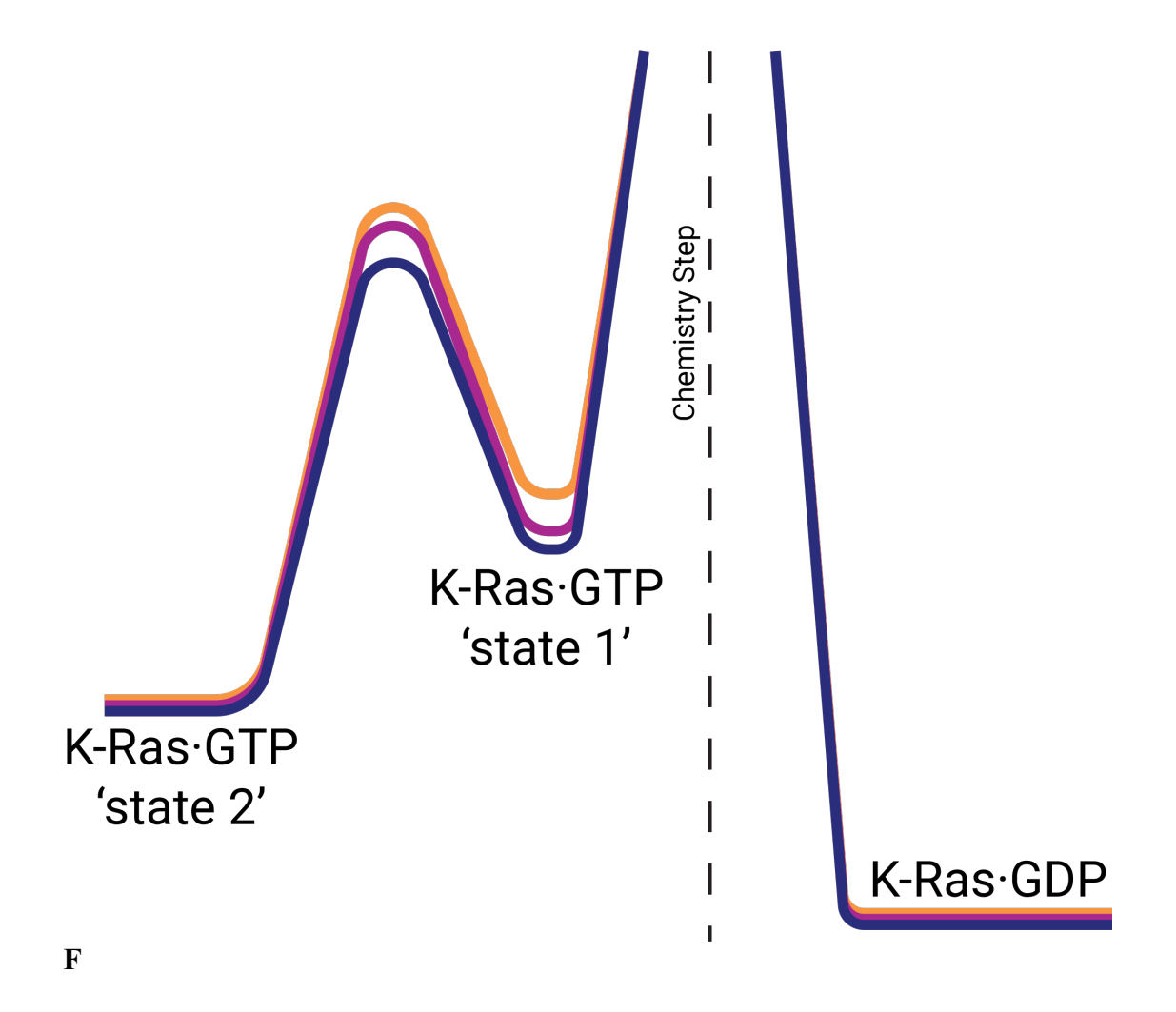


Figure 4. Backbone dynamics of K-Ras·GTP (filled circles) and K-Ras·GDP (open circles) for WT (dark blue) and its mutants G12D (purple) and G12C (orange) on the ps – μs timescales and secondary structure propensities (SSP). Secondary structural elements are shown at the top of the figure with the P-loop, Switch I and Switch II regions shaded in the panels as light yellow, red, and blue, respectively. **A)** Backbone N-H S^2 order parameters that were determined by the NASR approach for K-Ras·GTP. Data are presented as best fit values ± one standard deviation. The error in the datapoints were determined through monte carlo simulation and standard error propagation. **B)** Same as A but determined for K-Ras·GDP. **C)** SSP of each variant derived from K-Ras·GTP 13 Cα and 13 Cβ chemical shifts. **D)** Same as C but derived for K-Ras·GDP.



igure 5. Free energy scheme of K-Ras along its GTPase reaction coordinate of WT (dark blue) in comparison with its oncogenic G12D (purple) and G12C mutants (orange).

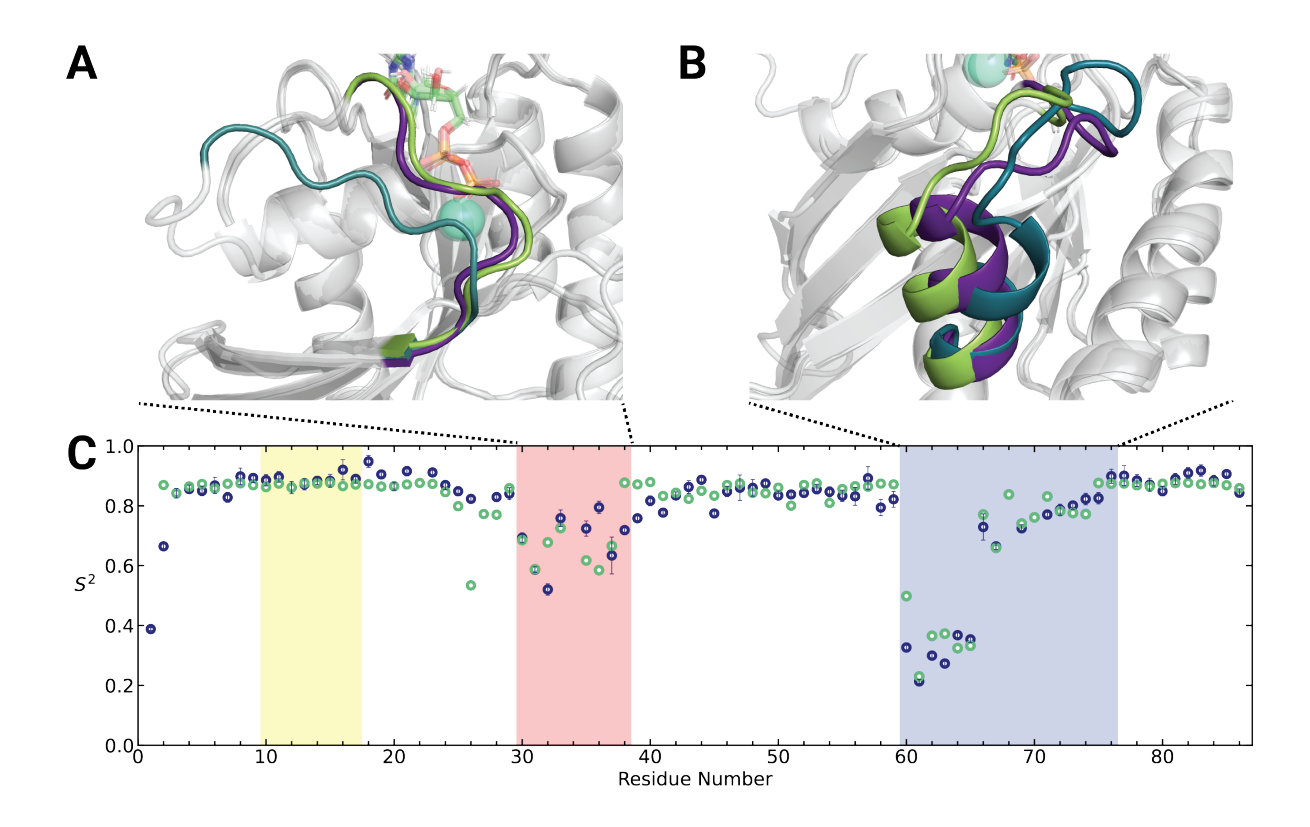


Figure 6. X-ray structure derived minimal ensemble of K-Ras·GDP Switch I and Switch II conformations and the back-calculated N-H S^2 order parameters. **A)** Backbone ribbon plots of those K-Ras·GDP crystal structures highlighting Switch I. **B)** The same crystal structures but highlighting Switch II. The ensemble consists of the WT K-Ras·GDP crystal structure (PDB entry 6MBU), the G12D mutant structure (PDB entry 4EPR (with engineered mutation C118S)), and the A59G mutant structure (PDB entry 6ASE). The GDP nucleotide is shown as sticks and Mg²⁺ as teal spheres. The Switch regions are indicated with non-gray colors (6MBU: green, 4EPR: dark purple, 6ASE: dark cyan). **C)** Comparison between the ensemble-derived backbone N-H S^2 order parameters (green) and the experimental S^2 (NASR) of WT K-Ras·GDP (dark blue). The S^2 (NASR) data are presented as the best fit \pm one standard deviation, as described in the caption of Figure 4. Populations of 47% (6MBU), 39% (4EPR), and 14% (6ASE) can best reproduce the experimental S^2 (NASR) result. The P-loop, Switch I, and Switch II regions are highlighted in yellow, red, and blue, respectively. The RMSDs between the ensemble-derived and experimental S^2 values are 0.12 for the Switch I region and 0.06 for the Switch II region.

References

- 1. Ellis, C. A. & Clark, G. The importance of being K-Ras. *Cell. Signal.* **12**, 425–434 (2000).
- 2. McCormick, F. A brief history of RAS and the RAS Initiative. *RAS Past, Present. Futur.* 1 (2022).
- 3. Marcus, K. & Mattos, C. Direct Attack on RAS: Intramolecular Communication and Mutation-Specific Effects. *Clin. Cancer Res.* **21**, 1810–1818 (2015).
- 4. Xu, S. *et al.* Structural insight into the rearrangement of the switch i region in GTP-bound G12A K-Ras. *Acta Crystallogr. Sect. D Struct. Biol.* **73**, 970–984 (2017).
- 5. Geyer, M. *et al.* Conformational transitions in p21(ras) and in its complexes with the effector protein Raf-RBD and the GTPase activating protein GAP. *Biochemistry* **35**, 10308–10320 (1996).
- 6. Spoerner, M. *et al.* Conformational states of human rat sarcoma (Ras) protein complexed with its natural ligand GTP and their role for effector interaction and GTP hydrolysis. *J. Biol. Chem.* **285**, 39768–39778 (2010).
- 7. Kalbitzer, H. R. & Spoerner, M. State 1(T) Inhibitors of Activated Ras. *Enzymes* **33**, 69–94 (2013).
- 8. Ito, Y. *et al.* Regional polysterism in the GTP-bound form of the human c-Ha-Ras protein. *Biochemistry* **36**, 9109–9119 (1997).
- 9. O'Connor, C. & Kovrigin, E. L. Global conformational dynamics in ras. *Biochemistry* **47**, 10244–10246 (2008).
- Long, D. *et al.* A comparative CEST NMR study of slow conformational dynamics of small GTPases complexed with GTP and GTP analogues. *Angew. Chem. Int. Ed. Engl.* 52, 10771–4 (2013).
- 11. Menyhárd, D. 'O. K. *et al.* Structural impact of GTP binding on downstream KRAS signaling. *Chem. Sci.* **11**, 9272–9289 (2020).
- 12. Chen, X. *et al.* Extending the Lifetime of Native GTP-Bound Ras for Site-Resolved NMR Measurements: Quantifying the Allosteric Dynamics. *Angew. Chemie* **131**, 2756–2759 (2019).

- 13. Parker, J. A., Volmar, A. Y., Pavlopoulos, S. & Mattos, C. K-Ras Populates Conformational States Differently from Its Isoform H-Ras and Oncogenic Mutant K-RasG12D. *Structure* **26**, 810-820.e4 (2018).
- 14. Palmer, A. G., Kroenke, C. D. & Loria, J. P. Nuclear magnetic resonance methods for quantifying microsecond-to-millisecond motions in biological macromolecules. *Methods Enzymol.* **339**, 204–38 (2001).
- 15. Vallurupalli, P., Sekhar, A., Yuwen, T. & Kay, L. E. Probing conformational dynamics in biomolecules via chemical exchange saturation transfer: a primer. *J. Biomol. NMR* **67**, 243–271 (2017).
- 16. Xie, M. *et al.* Functional protein dynamics on uncharted time scales detected by nanoparticle-assisted NMR spin relaxation. *Sci. Adv.* **5**, eaax5560 (2019).
- 17. Lipari, G. & Szabo, A. Model-free approach to the interpretation of nuclear magnetic resonance relaxation in macromolecules. 1. Theory and range of validity. *J. Am. Chem. Soc.* **104**, 4546–4559 (1982).
- 18. Vallurupalli, P., Bouvignies, G. & Kay, L. E. Studying 'invisible' excited protein states in slow exchange with a major state conformation. *J. Am. Chem. Soc.* **134**, 8148–8161 (2012).
- 19. Nielsen, J. T. & Mulder, F. A. A. Potenci: Prediction of temperature, neighbor and phcorrected chemical shifts for intrinsically disordered proteins. *J. Biomol. NMR* **70**, 141– 165 (2018).
- 20. Marsh, J. A., Singh, V. K., Jia, Z. & Forman-Kay, J. D. Sensitivity of secondary structure propensities to sequence differences between α- and γ-synuclein: Implications for fibrillation. *Protein Sci.* **15**, 2795–2804 (2006).
- 21. Shen, Y. & Bax, A. Protein structural information derived from nmr chemical shift with the neural network program talos-n. *Methods Mol. Biol.* **1260**, 17–32 (2015).
- Spoerner, M., Herrmann, C., Vetter, I. R., Kalbitzer, H. R. & Wittinghofer, A. Dynamic properties of the Ras switch I region and its importance for binding to effectors. *Proc. Natl. Acad. Sci.* 98, 4944–4949 (2001).

- 23. Linnemann, T. *et al.* Thermodynamic and kinetic characterization of the interaction between the Ras binding domain of AF6 and members of the Ras subfamily. *J. Biol. Chem.* **274**, 13556–13562 (1999).
- 24. Spoerner, M., Wittinghofer, A. & Kalbitzer, H. R. Perturbation of the conformational equilibria in Ras by selective mutations as studied by 31P NMR spectroscopy. *FEBS Lett.* **578**, 305–310 (2004).
- 25. Liao, J. *et al.* Two conformational states of Ras GTPase exhibit differential GTP-binding kinetics. *Biochem. Biophys. Res. Commun.* **369**, 327–332 (2008).
- 26. Johnson, C. W. & Mattos, C. The Allosteric Switch and Conformational States in Ras GTPase Affected by Small Molecules. *Enzymes* **33**, 41–67 (2013).
- 27. Fetics, S. K. *et al.* Allosteric Effects of the Oncogenic RasQ61L Mutant on Raf-RBD. *Structure* **23**, 505–516 (2015).
- 28. Pálfy, G. *et al.* The Importance of Mg2+-Free State in Nucleotide Exchange of Oncogenic K-Ras Mutants. *Chem. A Eur. J.* **28**, e202201449 (2022).
- 29. Hunter, J. C. *et al.* In situ selectivity profiling and crystal structure of SML-8-73-1, an active site inhibitor of oncogenic K-Ras G12C. *Proc. Natl. Acad. Sci. U. S. A.* **111**, 8895–8900 (2014).
- 30. Dharmaiah, S. *et al.* Structures of N-terminally processed KRAS provide insight into the role of N-acetylation. *Sci. Reports 2019 91* **9**, 1–15 (2019).
- 31. Sun, Q. *et al.* Discovery of Small Molecules that Bind to K-Ras and Inhibit Sos-Mediated Activation. *Angew. Chemie Int. Ed.* **51**, 6140–6143 (2012).
- 32. Pantsar, T. The current understanding of KRAS protein structure and dynamics. *Comput. Struct. Biotechnol. J.* **18**, 189–198 (2020).
- 33. Lu, J., Bera, A. K., Gondi, S. & Westover, K. D. KRAS Switch Mutants D33E and A59G Crystallize in the State 1 Conformation. *Biochemistry* **57**, 324–333 (2018).
- 34. Moghadamchargari, Z. *et al.* Intrinsic GTPase Activity of K-RAS Monitored by Native Mass Spectrometry. *Biochemistry* **58**, 3396–3405 (2019).
- 35. White, Y. et al. KRAS insertion mutations are oncogenic and exhibit distinct functional

- properties. *Nat. Commun.* 7, 1–8 (2016).
- 36. Boehr, D. D., Dyson, H. J., Wright, P. E., Boehr, D. D. & Wright, P. E. An NMR perspective on enzyme dynamics. *Chem. Rev.* **106**, 3055–79 (2006).
- 37. Baldwin, A. J. & Kay, L. E. NMR spectroscopy brings invisible protein states into focus. *Nat. Chem. Biol.* **5**, 808–14 (2009).
- 38. Eisenmesser, E. Z., Bosco, D. A., Akke, M. & Kern, D. Enzyme dynamics during catalysis. *Science* (80-.). **295**, 1520–1523 (2002).
- 39. Boehr, D. D., Nussinov, R. & Wright, P. E. The role of dynamic conformational ensembles in biomolecular recognition. *Nat. Chem. Biol.* 2009 511 **5**, 789–796 (2009).
- 40. Boehr, D. D., McElheny, D., Dyson, H. J., Wrightt, P. E. & Wright, P. E. The dynamic energy landscape of dihydrofolate reductase catalysis. *Science* **313**, 1638–42 (2006).
- 41. Peng, Y. *et al.* The Michaelis Complex of Arginine Kinase Samples the Transition State at a Frequency That Matches the Catalytic Rate. *J. Am. Chem. Soc.* **139**, 4846–4853 (2017).
- 42. Smith, M. J., Neel, B. G. & Ikura, M. NMR-based functional profiling of RASopathies and oncogenic RAS mutations. *Proc. Natl. Acad. Sci. U. S. A.* **110**, 4574–4579 (2013).
- 43. Tran, T. H. *et al.* KRAS interaction with RAF1 RAS-binding domain and cysteine-rich domain provides insights into RAS-mediated RAF activation. *Nat. Commun.* 2021 121 12, 1–16 (2021).
- 44. Lu, S. *et al.* Ras Conformational Ensembles, Allostery, and Signaling. *Chem. Rev.* **116**, 6607–6665 (2016).
- 45. Kobayashi, C. & Saito, S. Relation between the Conformational Heterogeneity and Reaction Cycle of Ras: Molecular Simulation of Ras. *Biophys. J.* **99**, 3726–3734 (2010).
- 46. Rudack, T., Xia, F., Schlitter, J., Korting, C. & Gerwert, K. Ras and GTPase-activating protein (GAP) drive GTP into a precatalytic state as revealed by combining FTIR and biomolecular simulations. *Proc. Natl. Acad. Sci. U. S. A.* **109**, 15295–15300 (2012).
- 47. Sayyed-Ahmad, A., Prakash, P. & Gorfe, A. A. Distinct dynamics and interaction patterns in H- and K-Ras oncogenic P-loop mutants. *Proteins Struct. Funct. Bioinforma.* **85**, 1618–1632 (2017).

- 48. Lukman, S., Grant, B. J., Gorfe, A. A., Grant, G. H. & McCammon, J. A. The Distinct Conformational Dynamics of K-Ras and H-Ras A59G. *PLOS Comput. Biol.* **6**, e1000922 (2010).
- 49. Pantsar, T. *et al.* Assessment of mutation probabilities of KRAS G12 missense mutants and their long-timescale dynamics by atomistic molecular simulations and Markov state modeling. *PLOS Comput. Biol.* **14**, e1006458 (2018).
- 50. Grudzien, P., Jang, H., Leschinsky, N., Nussinov, R. & Gaponenko, V. Conformational Dynamics Allows Sampling of an "Active-like" State by Oncogenic K-Ras-GDP. *J. Mol. Biol.* **434**, 167695 (2022).
- 51. S, U. K., R, B., D, T. K., Doss, C. G. P. & Zayed, H. Mutational landscape of K-Ras substitutions at 12th position-a systematic molecular dynamics approach. *J. Biomol. Struct. Dyn.* **40**, 1571–1585 (2022).
- 52. Zeng, J. *et al.* Identification of functional substates of KRas during GTP hydrolysis with enhanced sampling simulations. *Phys. Chem. Chem. Phys.* **24**, 7653–7665 (2022).
- 53. Li, D. W. & Brüschweiler, R. Certification of molecular dynamics trajectories with NMR chemical shifts. *J. Phys. Chem. Lett.* **1**, 246–248 (2010).
- 54. Liu, D., Mao, Y., Gu, X., Zhou, Y. & Long, D. Unveiling the 'invisible' druggable conformations of GDP-bound inactive Ras. *Proc. Natl. Acad. Sci. U. S. A.* **118**, e2024725118 (2021).

Methods

Human K-Ras4B G-domain cloning and expression

The wild-type of the G-domain of human K-Ras4B (residues 1-169), referred to as K-Ras, was subcloned by PCR amplification of the corresponding DNA sequence from a plasmid into an expression vector pTBSG1⁵⁵ and verified by Sanger sequencing. pTBSG1_kRaswt plasmid was used as the template to generate pTBSG1_kRasG12C and pTBSG1_kRasG12D plasmids using a site-directed mutagenesis kit (Agilent). Sanger sequencing was subsequently used to verify the correct DNA coding sequences. All three plasmids were individually transformed into *E. coli* strain BL21(DE3) for protein over-expression and uniform isotope ¹⁵N or ¹⁵N-¹³C for NMR measurements. The oligonucleotide sequences of all K-Ras constructs (WT, G12C, G12D) are given in **Table S3**.

Protein expression of all three forms of the K-Ras G domain was carried out in M9 minimal media. For U-¹⁵N labeling, ¹⁵N NH₄Cl (1 g/L) was used as sole nitrogen source and for (U-¹⁵N, U-¹³C)-double labeling, ¹⁵N NH₄Cl (1 g/L) and ¹³C glucose (4g/L) were used as sole nitrogen and carbon source, respectively. Isotopes were purchased either from CIL or Isotech. *E. coli* culture was grown at 37°C to OD 0.7 and induced by IPTG (Fisher Scientific) overnight at 25°C. Protein purification was performed as described previously⁵⁵.

NMR sample preparation

For the preparation of K-Ras·GDP samples, purified protein was buffer exchanged with a centrifugal filter (Amicon Ultra, MWCO 3kDa) in 20 mM HEPES buffer (pH 7.0) and concentrated to 650-750 μ M, supplemented with 5 mM GDP (Sigma), 5 mM MgCl₂, 5 mM BME, and 5% D₂O for NMR measurements.

For the preparation of K-Ras·GTP samples, purified protein was buffer exchanged first in 20 mM HEPES and 15 mM EDTA buffer (pH 7.0), followed by another buffer exchange in 20 mM HEPES buffer (pH 7.0) before being concentrated. After the protein concentration was measured, the protein solution was diluted to $100 \, \mu M$ with 20 mM HEPES buffer (pH 7.0), and GTP ligand (Fisher Scientific) was added to a final concentration of $10 \, mM$ for further buffer

exchange, a step that was then repeated twice. The final, concentrated protein solution (650-750 µM) was supplemented with 5 mM MgCl₂, 5 mM BME, and 5% D₂O for NMR measurements.

Resonance assignments

NMR spectra for the sequence-specific NMR resonance assignments were recorded on a Bruker Avance III 850 MHz spectrometer (Bruker, Billerica, MA), equipped with a 5 mm TCI triple resonance HCN cryoprobe and Z-axis gradient. A series of six standard triple-resonance experiments (Sattler et al., 1999) was subsequently recorded using sensitivity-enhanced gradient coherence selection^{56,57}, semi-constant time acquisition in the ¹⁵N dimension⁵⁸, and non-uniform sampling (NUS) following a Poisson-gap sampling schedule.⁵⁹ Additionally, 3D ¹⁵N-edited NOESY and 3D CNH-NOESY⁶⁰ were recorded using uniform sampling with a mixing time of 180 ms. Full details are provided in Supporting Information. Experiments were started on freshly purified samples and each sample took between 9 and 10 days for completion. Combined application of these methods made it possible to assign essentially all residues in Switch I and Switch II for all K-Ras GTP samples. The experimental temperature was kept at 298 K for the protein samples in complex with GDP, at 288 K for K-Ras(G12C)·GTP, and at 283 K for K-Ras(WT)·GTP and K-Ras(G12D)·GTP. To aid the transfer of the backbone NH assignments to room temperature, 3D HNCO experiments were then repeated at 298 K on these GTP-bound samples. All the data were processed using NMRPipe⁶¹/SMILE⁶² and visualized using NMRViewJ⁶³ both via NMRBox⁶⁴. Secondary structure propensity calculations of the three variants in their GDP- and GTP-bound forms were performed using the program SSP²⁰ and TALOS-N²¹.

Relaxation Dispersion Experiments and Nanoparticle-assisted Relaxation

Backbone amide ¹⁵N and ¹H^N CPMG NMR relaxation dispersion experiments at 298 K were acquired on 850 and 600 MHz NMR instruments and amide ¹⁵N CEST¹⁸ experiments were performed for all samples on the 850 MHz instrument using a CEST mixing time of 150 ms and B₁ field strengths as listed in **Table S1** (see Supplementary Information). All dynamics experiments were performed on freshly purified K-Ras·GTP samples and used for no more than 3 days before being replaced with a sample from the same batch and identical buffer that had been kept at 4°C. CPMG and CEST profiles were analyzed collectively using ChemEx¹⁸ and all three

GTP-bound variants fit to a model of two-site exchange. Bootstrap analyses were performed to determine the experimental errors in the fitted parameters. For interpretation of the results, random coil chemical shifts were predicted from the amino-acid sequences of Switch I and Switch II using the software POTENCI¹⁹.

For all nanoparticle-assisted spin relaxation experiments (NASR), Levasil CS40-120 colloidal anionic silica nanoparticles (SNPs) with an average diameter of 20 nm⁶⁵ (obtained from NouryonTM) were dialyzed and directly mixed into the protein-containing buffer. The final concentrations of SNPs in the NMR samples were between 0.5 and 1.5 μ M. Backbone amide ¹⁵N R_1 and R_2 spin relaxation rates for samples both in the absence and presence of SNPs were measured at 850 MHz NMR magnetic field strength using standard ¹⁵N R_1 and $R_{1\rho}$ relaxation experiments^{66,67} as described previously¹⁶ and analyzed as described in **Supplementary Information**.

Data Availability

NMR backbone resonance assignments of K-Ras·GTP WT, G12D, and G12C have been deposited in the publicly accessible BMRB database (https://bmrb.io/) under accession codes 52021, 52023, and 52024. All relaxation dispersion, CEST, and NASR results can be accessed at doi:10.5061/dryad.j6q573nm0.

Methods-only references

- 55. Showalter, S. A., Bruschweiler-Li, L., Johnson, E., Zhang, F. & Brüschweiler, R. Quantitative lid dynamics of MDM2 reveals differential ligand binding modes of the p53-binding cleft. *J. Am. Chem. Soc.* **130**, 6472–6478 (2008).
- 56. Palmer, A. G., Cavanagh, J., Wright, P. E. & Rance, M. Sensitivity improvement in proton-detected two-dimensional heteronuclear correlation NMR spectroscopy. *J. Magn. Reson.* **93**, 151–170 (1991).
- 57. Schleucher, J. *et al.* A general enhancement scheme in heteronuclear multidimensional NMR employing pulsed field gradients. *J. Biomol. NMR* **4**, 301–306 (1994).
- 58. Grzesiek, S. & Bax, A. Amino acid type determination in the sequential assignment procedure of uniformly 13C/15N-enriched proteins. *J. Biomol. NMR* 1993 32 3, 185–204

(1993).

- 59. Hyberts, S. G., Takeuchi, K. & Wagner, G. Poisson-gap sampling and forward maximum entropy reconstruction for enhancing the resolution and sensitivity of protein NMR data. *J. Am. Chem. Soc.* **132**, 2145–2147 (2010).
- 60. Diercks, T., Coles, M. & Kessler, H. An efficient strategy for assignment of cross-peaks in 3D heteronuclear NOESY experiments. *J. Biomol. NMR* 1999 152 **15**, 177–180 (1999).
- 61. Delaglio, F. *et al.* NMRPipe: a multidimensional spectral processing system based on UNIX pipes. *J. Biomol. NMR* **6**, 277–93 (1995).
- 62. Ying, J., Delaglio, F., Torchia, D. A. & Bax, A. Sparse multidimensional iterative lineshape-enhanced (SMILE) reconstruction of both non-uniformly sampled and conventional NMR data. *J. Biomol. NMR* **68**, 101–118 (2017).
- 63. Johnson, B. A. & Blevins, R. A. NMR View: A computer program for the visualization and analysis of NMR data. *J. Biomol. NMR 1994 45* **4**, 603–614 (1994).
- 64. Maciejewski, M. W. *et al.* NMRbox: A Resource for Biomolecular NMR Computation. *Biophys. J.* **112**, 1529–1534 (2017).
- 65. Zhang, B., Xie, M., Bruschweiler-Li, L., Bingol, K. & Brüschweiler, R. Use of Charged Nanoparticles in NMR-Based Metabolomics for Spectral Simplification and Improved Metabolite Identification. *Anal. Chem.* 87, 7211–7217 (2015).
- 66. Lakomek, N. A., Ying, J. & Bax, A. Measurement of 15N relaxation rates in perdeuterated proteins by TROSY-based methods. *J. Biomol. NMR* **53**, 209–221 (2012).
- 67. Gairí, M. *et al.* An optimized method for 15N R1 relaxation rate measurements in non-deuterated proteins. *J. Biomol. NMR* **62**, 209–220 (2015).